Chemical Science

ROYAL SOCIETY OF CHEMISTRY

EDGE ARTICLE

View Article Online
View Journal | View Issue

Check for updates

Cite this: *Chem. Sci.*, 2026, **17**, 4518

All publication charges for this article have been paid for by the Royal Society of Chemistry

Open Access Article. Published on 02 2026. Downloaded on 28/05/2026 05:22:51.
This article is licensed under a Creative Commons Attribution-NonCommercial 3.0 Unported Licence.

Photocatalytic CO_2 reduction using a diazabenzacenaphthenium photosensitizer and a Mn catalyst

Kei Kamogawa, *[a] Shintaro Okumura *[b] and Osamu Ishitani *[a]

Redox photosensitizers are key components in photoredox catalysis, mediating photoinduced electron transfer from an electron donor to a catalyst or substrate. In systems proceeding through reductive quenching, the efficiency of forming the one-electron-reduced photosensitizer critically determines the overall quantum yield. Here, we report a comprehensive photophysical investigation of 4,5,9,10-tetraethyl-1,2-dihydrobenz[*de*]imidazo[1,2,3-*ij*]-1,8-naphthridinium cation (***N*-BAP$^+$**), originally developed as a redox photosensitizer for oxidative quenching in photocatalytic organic synthesis. The photochemical reduction of ***N*-BAP$^+$** by 1,3-dimethyl-2-phenyl-2,3-dihydro-1*H*-benzo[*d*]imidazole (BIH) was also analyzed, focusing on the contributions of the singlet and triplet excited states of ***N*-BAP$^+$**. Spectroscopic studies demonstrate that ***N*-BAP$^+$** undergoes efficient reductive quenching with BIH, generating the one-electron-reduced species ***N*-BAP$^{\bullet}$**. Based on these findings, we applied ***N*-BAP$^+$** to photocatalytic CO_2 reduction using a Mn–complex catalyst and BIH as a reductant, resulting in an efficient and durable photocatalytic CO_2 reduction system. Kinetic analysis revealed that the reductive quenching of the triplet excited state was the essential pathway governing the activity of this photocatalytic CO_2 reduction. These findings suggest that numerous candidates, with or without TADF properties, could serve as organic redox photosensitizers free of heavy metal ions. For optimal performance, such molecules should achieve as high a triplet excited-state formation yield as possible while keeping the singlet excited-state lifetime as short as possible.

Received 7th November 2025
Accepted 1st January 2026

DOI: 10.1039/d5sc08659k

rsc.li/chemical-science

Introduction

Redox photosensitizers are frequently used in various photocatalytic reactions, especially in the fields of artificial photosynthesis[1–5] and organic synthesis.[6–9] The photosensitizer absorbs light to transfer an electron from an electron donor to an acceptor as shown in Scheme 1a. Since this redox photosensitized process initiates various photocatalytic reactions, the selection of a photosensitizer has a critical effect on the overall efficiency of photocatalytic reactions.

Recently, in addition to transition metal complexes, organic dyes have been actively investigated as photosensitizers. For example, several organic TADF (thermally activated delayed fluorescence) dyes are suitable as photosensitizers because they exhibit strong UV-vis absorption, appropriate electrochemical properties, and long-lived triplet excited states with high yields.[10–13] Many organic photosensitizers differ significantly from conventional heavy-metal-based photosensitizers. For example, the singlet metal-to-ligand charge transfer (^{1}MLCT) excited state of $[Ru(diimine)_3]^{2+}$ is rapidly converted to the triplet (^{3}MLCT) excited state within approximately 100 fs *via* intersystem crossing (ISC), and only the ^{3}MLCT excited state contributes to photocatalytic reactions.[14] In contrast, since the ISC rates from the singlet to the triplet excited states of organic molecules are mostly much slower, both singlet and triplet excited states can be quenched by an electron donor and/or acceptor. For instance, the rate constants of ISC of 2,4,5,6-tetrakis(diphenylamino)-isophthalonitrile (**4DPAIPN**) and 2,4,6-tri(diphenylamino)-5-fluoroisophthalonitrile (**3DPAFIPN**), which have been employed as efficient TADF organic photosensitizers for photocatalytic CO_2 reduction, are 2.9×10^8 s^{-1} and 1.5×10^8 s^{-1}, respectively.[15] These rates are slow enough to compete with dynamic quenching of their singlet excited states in solution. Recently, our group reported that reductive quenching of the triplet excited state of these TADF organic photosensitizers by 1,3-dimethyl-2-phenyl-2,3-dihydro-1*H*-benzo[*d*]imidazole (BIH) affords a triplet geminate radical ion pair, which experiences a slower backward electron transfer affording the ground state than the corresponding singlet geminate radical ion pair.[15] The escape yield from the triplet geminate radical ion pair is approximately 10 times higher than that from the singlet state. The significant difference is

[a]*Department of Chemistry, Graduate School of Advanced Science and Engineering, Hiroshima University, 1-3-1 Kagamiyama, Higashi-Hiroshima, Hiroshima 739-8526, Japan. E-mail: kamokei@hiroshima-u.ac.jp; iosamu@hiroshima-u.ac.jp*

[b]*Department of Synthetic Chemistry and Biological Chemistry, Kyoto University, Katsura, Kyoto 615-8510, Japan. E-mail: okumura.shintaro.6e@kyoto-u.ac.jp*

© 2026 The Author(s). Published by the Royal Society of Chemistry

Open Access Article. Published on 02 2026. Downloaded on 28/05/2026 05:22:51.
This article is licensed under a Creative Commons Attribution-NonCommercial 3.0 Unported Licence.

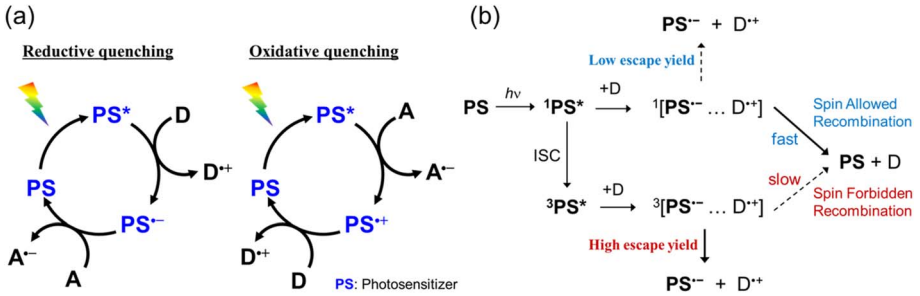

Scheme 1 (a) Redox photosensitized reactions. (b) Reductive quenching processes of the singlet and triplet excited states of a redox photosensitizer by an electron donor and backward electron transfer in the produced geminate radical pairs.

attributed to the spin selection rule on the charge recombination processes: the spin-forbidden nature of the charge recombination within the triplet geminate radical pair results in slower recombination and higher escape yield (Scheme 1b).[16] Therefore, in photoredox reactions employing organic photosensitizers, it is essential to investigate in detail the reactivities of both the singlet and triplet excited states.

There are several reports on efficient photocatalytic CO_2 reduction reactions employing organic photosensitizers that are not TADF dyes, such as anthraquinone derivatives,[17–19] phenoxazine derivatives,[20,21] acriflavine derivatives,[22,23] and triazatriangulenium salts.[24–26] However, in these organic photosensitizers, the relative contributions of the singlet and triplet excited states to the reactions, including the influence of the spin multiplicity of the excited states on the quantum yield of the photocatalytic reaction, have not been quantitatively evaluated. Transient absorption spectroscopy should be an effective method for probing the photoreactivity of triplet excited states in such photosensitizers that lack both TADF and room-temperature phosphorescence.

4,5,9,10-Tetraethyl-1,2-dihydrobenz[*de*]imidazo[1,2,3-*ij*]-1,8-naphthridinium cation (***N*-BAP**$^+$ in Chart 1) also acts as a photosensitizer without the TADF properties owing to relatively large energy gap between the singlet and triplet excited states (ΔE_{ST} = 290 meV). Its excited states (E^*_{ox} = –1.71 V (S_1) and − 1.42 V (T_1) *vs.* SCE) and one-electron reduced species ($E_{p,red}$ = −1.89 V) exhibit strong reducing power. Owing to this reducing ability and intense visible-light absorption, ***N*-BAP**$^+$ functions as a redox photosensitizer for visible-light-driven four-electron reduction of esters to generate a carbinol anion intermediate.[27] Although the high durability and strong reducing power of ***N*-BAP**$^+$ suggest its potential applicability to photocatalytic reduction of CO_2, such systems have not been reported yet, and the photophysical properties of ***N*-BAP**$^+$, particularly the photoreactivity of its triplet excited state, have not been thoroughly investigated.

Herein, we report detailed photophysical properties of ***N*-BAP**$^+$, including the rates associated with ISC and the yield of its triplet excited state. The reductive quenching processes of the singlet and triplet excited states of ***N*-BAP**$^+$ by BIH were also thoroughly investigated. Because ***N*-BAP**$^+$ does not exhibit delayed fluorescence or room-temperature phosphorescence, the dynamics of these photophysical and photochemical processes were investigated in detail using transient absorption spectroscopy, in contrast to previous studies on TADF organic photosensitizers that relied on emission-decay analysis. Based on these findings, we successfully developed a new photocatalytic system for CO_2 reduction employing ***N*-BAP**$^+$ as a redox photosensitizer, *fac*-[Mn^I(6-mesityl-4,4′-dimethyl-2,2′-bipyridine)(CO)$_3$(OC(O)OCH$_2$CF$_3$)] (**MnMes** in Chart 1) as a catalyst, and BIH as an electron donor, in which ***N*-BAP**$^+$ exhibited remarkable durability and effectively functioned as a redox photosensitizer for the selective reduction of CO_2 to CO. Furthermore, we constructed a kinetic model for the reductive quenching of the singlet and triplet excited states in non-TADF molecules and examined how the spin multiplicity of the excited state influences the photocatalytic activity for CO_2 reduction.

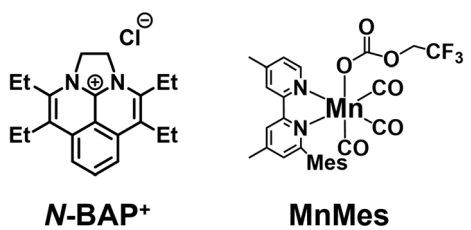

***N*-BAP**$^+$ **MnMes**

Chart 1 Structures of *N*-BAP$^+$ and MnMes.

Results and discussion

Photophysical properties of *N*-BAP$^+$

***N*-BAP**$^+$ exhibited a strong absorption band at λ_{max} = 441 nm (ε = 9200 M^{-1} cm^{-1}) with a vibronic structure in a DMSO solution containing 3.78 M trifluoroethanol (TFE) (Fig. 1a). This mixed solvent was used for the photocatalytic CO_2 reduction described later. Fluorescence was observed at λ_{max} = 452 nm at room temperature. The fluorescence lifetime (τ_f) and quantum yield (Φ_f) were determined to be 5.6 ns and 33%, respectively, under Ar (Fig. 1b and Table 1). The fluorescence lifetime was marginally reduced under air (5.3 ns), indicating minor quenching by O_2. Although ***N*-BAP**$^+$ exhibits phosphorescence at 77 K,[27] phosphorescence was not detected at room temperature.

To gain deeper insight into the excited-state dynamics of ***N*-BAP**$^+$, particularly the triplet excited state, ns-transient

Open Access Article. Published on 02 2026. Downloaded on 28/05/2026 05:22:51.
This article is licensed under a Creative Commons Attribution-NonCommercial 3.0 Unported Licence.

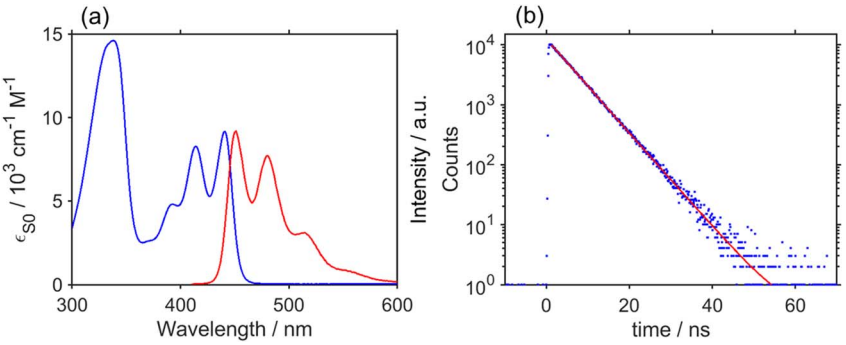

Fig. 1 (a) UV-vis absorption spectrum (blue) and fluorescence spectrum (red) of ***N*-BAP**$^+$ in a DMSO solution containing 3.78 M TFE. λ_{ex} = 390 nm. (b) Fluorescence decay of ***N*-BAP**$^+$ in an Ar-purged DMSO solution containing 3.78 M TFE with the corresponding kinetic fit (red line). λ_{ex} = 444 nm, λ_{det} = 480 nm.

Table 1 Photophysical properties of ***N*-BAP**$^+$ in an Ar-purged DMSO solution containing 3.78 M TFE

$\tau_f{}^a$/ns	$\Phi_f{}^b$/%	Φ_{ISC}/%	$k_r/10^8$ s^{-1}	$k_{nr}/10^8$ s^{-1}	$k_{ISC}/10^8$ s^{-1}
5.3^c, 5.6^d	33	57	0.59	0.19	1.0

^{a} λ_{ex} = 444 nm, λ_{det} = 480 nm. ^{b} λ_{ex} = 400 nm. ^{c} Under air. ^{d} Under Ar.

absorption (TA) measurements were performed. Fig. 2a shows the TA spectra of ***N*-BAP**$^+$ in an Ar-purged DMSO–TFE mixed solution following pulsed excitation at 355 nm. The spectra were globally analyzed using a two-component sequential model (Fig. 2b and c).[28,29] The evolution-associated spectra (EAS) shown in Fig. 2b represent the spectral profiles of transient species associated with each kinetic component. The first component (EAS1) exhibited intense absorption at $\lambda_{max} \approx$ 660 nm with a shoulder near 610 nm. This state was converted to the second component (EAS2) with a time constant of 5.7 ns. Because this time constant matches the fluorescence lifetime (Fig. 1b), EAS1 is attributed to the singlet excited state (^{1}***N*-BAP**$^+$). The second component displayed broad absorption at $\lambda_{max} \approx$ 620 nm and a long lifetime (>10 μs). Under aerobic conditions, the decay of this component was significantly accelerated, while the decay of the first component was only marginally affected, suggesting that EAS2 corresponds to the triplet excited state (^{3}***N*-BAP**$^+$) (Fig. S1). Furthermore, the calculated T–T absorption spectrum of ^{3}***N*-BAP**$^+$ closely matches that of EAS2 (Fig. S2). Based on these results, EAS2 is assigned to ^{3}***N*-BAP**$^+$. Therefore, a fraction of the photochemically generated ^{1}***N*-BAP**$^+$ is converted to ^{3}***N*-BAP**$^+$ *via* ISC even at room temperature.

The quantum yield of ISC (Φ_{ISC}) was determined to be 57% using a relative actinometry method (see SI for details);[30–32] Φ_{ISC} was calculated by comparing the triplet-excited-state yield of ***N*-BAP**$^+$ with that of a reference solution containing $[Ru(bpy)_3]Cl_2$, whose ISC quantum yield ($\Phi_{ISC,Ru}$) is close to unity,[14,33] with both solutions excited by 355 nm laser light of identical intensity (eqn (1)).

$$\Phi_{ISC} = \Phi_{ISC,Ru} \times \frac{[^3\textbf{\textit{N}}\textbf{-BAP}^+]}{[^3Ru^*]} \times \frac{1 - 10^{-A_{Ru}}}{1 - 10^{-A_{N\text{-}BAP^+}}} \quad (1)$$

where [^{3}***N*-BAP**$^+$] and [^{3}Ru*] represent the concentrations of photogenerated ^{3}***N*-BAP**$^+$ and the ^{3}MLCT excited state of $[Ru(bpy)_3]Cl_2$, respectively; and $A_{N\text{-}BAP+}$ and A_{Ru} denote the absorbance at 355 nm (excitation wavelength) for solutions containing ***N*-BAP**$^+$ or $[Ru(bpy)_3]Cl_2$, respectively. Furthermore,

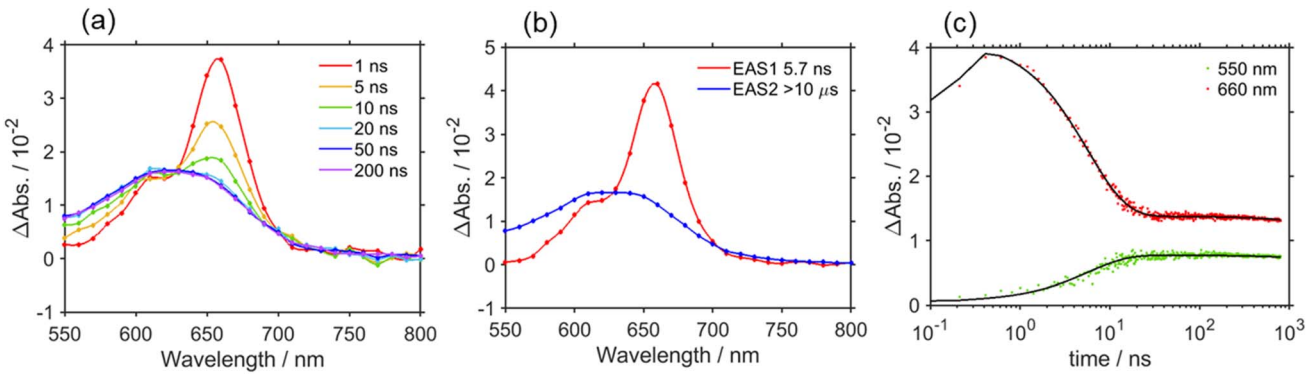

Fig. 2 (a) TA spectra of an Ar-purged DMSO solution containing ***N*-BAP**$^+$ (0.4 mM) and TFE (3.78 M) after pulsed excitation at λ_{ex} = 355 nm (100 Hz, 17 μJ per pulse). (b) Evolution-associated spectra (EAS) generated by global analysis of the TA spectra using a two-component sequential model. (c) Kinetic traces (dots) of transient absorption spectra at characteristic wavelengths with their fits (black lines).

© 2026 The Author(s). Published by the Royal Society of Chemistry

Open Access Article. Published on 02 2026. Downloaded on 28/05/2026 05:22:51.
This article is licensed under a Creative Commons Attribution-NonCommercial 3.0 Unported Licence.

using eqn (2)–(4), the rate constants for radiative (k_r) and non-radiative (k_{nr}) decay of ^{1}***N*-BAP$^+$** and for ISC (k_{ISC}) were calculated to be 5.9×10^7, 1.9×10^7, and 1.0×10^8 s^{-1}, respectively (Table 1).

$$\tau_f^{-1} = k_r + k_{nr} + k_{ISC} \quad (2)$$

$$\Phi_f = k_r \tau_f \quad (3)$$

$$\Phi_{ISC} = k_{ISC} \tau_f \quad (4)$$

As described above, photoexcitation of ***N*-BAP$^+$** generates both ^{1}***N*-BAP$^+$** and ^{3}***N*-BAP$^+$**. Although their lifetimes differ, both are sufficiently long to enable bimolecular reactions *via* diffusion in solution and they exhibit substantial photo-oxidation power ($E^*_{red}(^1$***N*-BAP$^+$**) = +0.90 V, $E^*_{red}(^3$***N*-BAP$^+$**) = +0.61 V *vs.* SCE).[27] Therefore, the reductive quenching processes of ^{1}***N*-BAP$^+$** and ^{3}***N*-BAP$^+$** were examined using 1,3-dimethyl-2-phenyl-2,3-dihydro-1*H*-benzo[*d*]imidazole (BIH), which is a commonly employed reductant in various photocatalytic reactions (E_{ox}(BIH) = +0.33 V).[34–37]

Reductive quenching of the excited *N*-BAP$^+$ by BIH

Fluorescence from ^{1}***N*-BAP$^+$** was quenched upon addition of BIH in a DMSO solution containing TFE (3.78 M) (Fig. S3). From the slope of the linear Stern–Volmer plot (K_{SV} = 20.9 M^{-1}) and the fluorescence lifetime (τ_f = 5.6 ns) under Ar, the quenching rate constant for ^{1}***N*-BAP$^+$** was determined to be $^1k_q = 3.8 \times 10^9$ M^{-1} s^{-1}. Because BIH has a much higher singlet excitation energy (E_{00} = 3.79 eV) than ^{1}***N*-BAP$^+$** (2.79 eV),[27,38] energy transfer can be ruled out as a possible quenching mechanism. Thus, we conclude that ^{1}***N*-BAP$^+$** is reductively quenched by BIH.

The quenching process of ^{3}***N*-BAP$^+$** by BIH was investigated using TA measurements because ***N*-BAP$^+$** does not exhibit phosphorescence and delayed fluorescence at room temperature. Fig. 3a shows the typical TA spectra of an Ar-purged DMSO solution containing ***N*-BAP$^+$** (0.4 mM), TFE (3.78 M), and BIH (1 mM) following pulsed excitation at 355 nm. In this experiment, the absorption of BIH at 355 nm was negligible owing to its low concentration, indicating that ***N*-BAP$^+$** was selectively excited by the pump pulse (Fig. S4). The reductive quenching of ^{1}***N*-BAP$^+$** by BIH was also negligible due to the low BIH concentration (only 2% of ^{1}***N*-BAP$^+$** is quenched in the presence of 1 mM of BIH; see eqn (6) described below). At 38 ns after pulsed excitation, when ISC is complete, the absorption band assigned to ^{3}***N*-BAP$^+$** was observed. The spectra were globally analyzed using a three-component sequential model (Fig. 3b and c).

The first component (EAS1), assigned to ^{3}***N*-BAP$^+$**, decayed rapidly with a time constant τ_1 = 1.0 μs, forming the second component (EAS2), which exhibited a weak and broad absorption band at $\lambda_{max} \approx$ 470 nm. τ_1 depends linearly on the BIH concentration between 0.5 mM and 2 mM, with a bimolecular rate constant of 1.0×10^9 M^{-1} s^{-1} (Fig. S5), indicating that ^{3}***N*-BAP$^+$** is dynamically quenched by BIH. Because the triplet excitation energy of BIH (3.04 eV) is much higher than that of ^{3}***N*-BAP$^+$** (2.50 eV),[27,38] we conclude that ^{3}***N*-BAP$^+$** is reductively quenched by BIH with the rate constant $^3k_q = 1.0 \times 10^9$ M^{-1} s^{-1}, forming the one-electron-reduced species ***N*-BAP$^\bullet$** and the one-electron-oxidized species **BIH$^{\bullet+}$**. The second component subsequently decayed, giving rise to the long-lived third component (EAS3) with a time constant τ_2 = 7.7 μs. The third

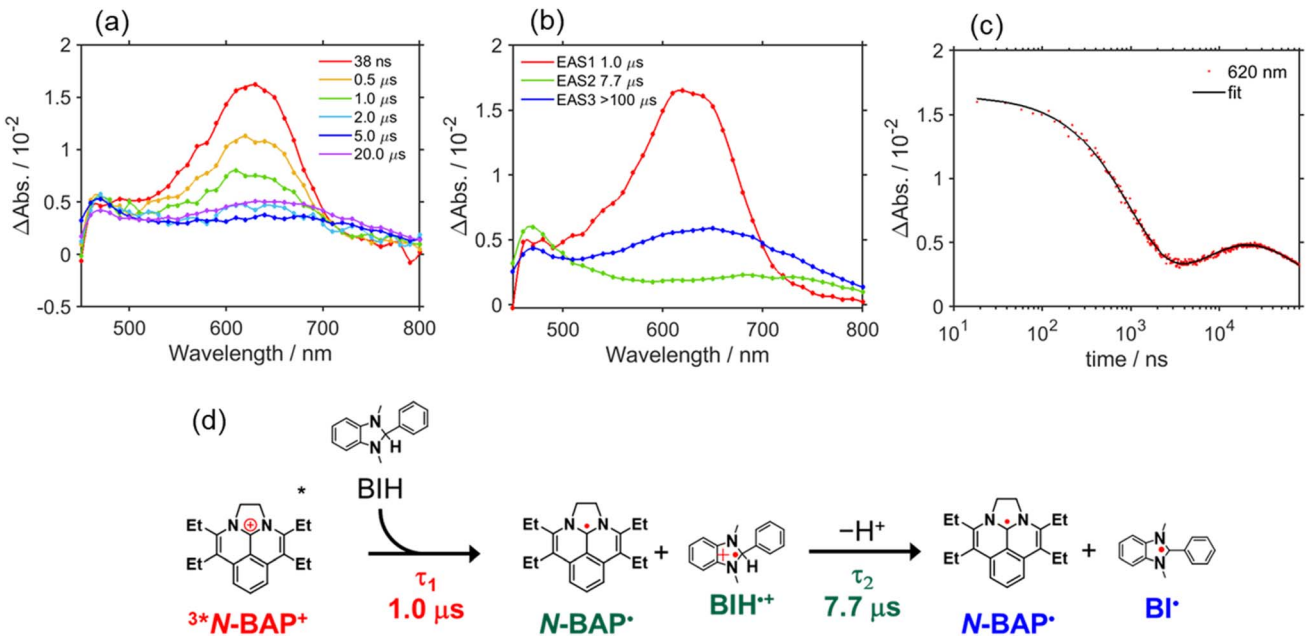

Fig. 3 (a) TA spectra of an Ar-purged DMSO solution containing ***N*-BAP$^+$** (0.4 mM), BIH (1 mM), and TFE (3.78 M) following pulsed excitation at λ_{ex} = 355 nm (50 Hz, 17 μJ per pulse). (b) Evolution-associated spectra (EAS) obtained by global analysis of the transient absorption spectra using a three-component sequential model. (c) Kinetic trace (dots) of transient absorption at 620 nm with the fitted curve (black line). (d) Mechanism for the reductive quenching of ^{3}***N*-BAP$^+$** by BIH.

Open Access Article. Published on 02 2026. Downloaded on 28/05/2026 05:22:51.
This article is licensed under a Creative Commons Attribution-NonCommercial 3.0 Unported Licence.

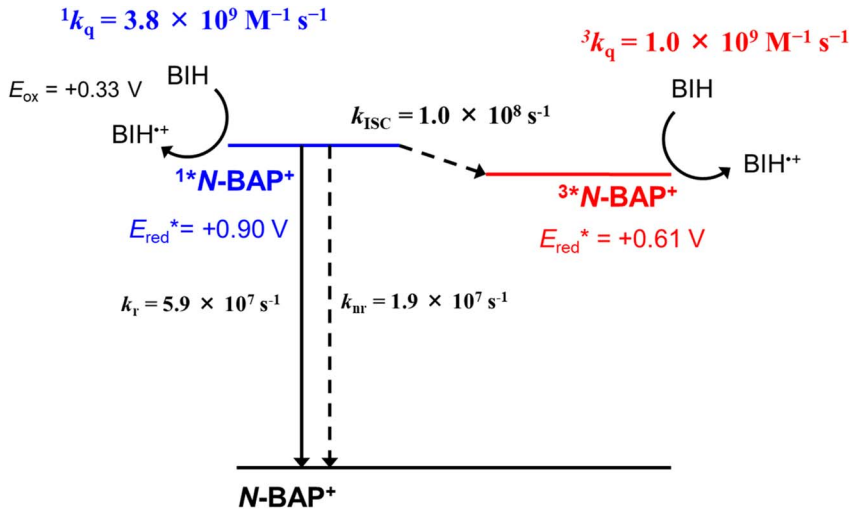

Scheme 2 Excited-state dynamics of *N*-BAP$^+$ in the presence of BIH.

component exhibited a broad absorption band at $\lambda_{max} \approx$ 650 nm, similar to the absorption spectrum of **BI**$^\bullet$, which is a deprotonated species of **BIH**$^{\bullet+}$ (Fig. 3d).[39,40] Therefore, EAS2 is attributed to the combined absorption of **BIH**$^{\bullet+}$ and ***N*-BAP**$^\bullet$, and EAS3 to those of **BI**$^\bullet$ and ***N*-BAP**$^\bullet$ (Fig. 3). Although **BI**$^\bullet$ has relatively strong reduction power ($E_{p,ox} = -1.68$ V *vs.* SCE),[41] it is insufficient to reduce ***N*-BAP**$^+$ in the ground state ($E_{p,red} = -1.89$ V *vs.* SCE), leading to **BI**$^\bullet$ accumulation during TA measurements. A much slower decay of EAS3 (>100 μs) was observed, likely due to decomposition and/or bond formation among accumulated radical species. It is noteworthy that these decomposition processes should not proceed in the photocatalytic reactions described below because both ***N*-BAP**$^\bullet$ and **BI**$^\bullet$ supply an electron to the catalyst (**MnMes**) and the intermediate(s) derived from **MnMes** owing to the strong reduction powers of these radical species.

Scheme 2 summarizes the rate constants for all processes following the excitation of ***N*-BAP**$^+$ in the presence of BIH. These experiments and kinetic analyses clearly demonstrate that both ^{1}***N*-BAP**$^+$ and ^{3}***N*-BAP**$^+$ can be reductively quenched by BIH, with large but distinct rate constants. Based on these results and the suitable redox potential of **MnMes** ($E_{p,red} = -1.12$ V *vs.* SCE),[42] we employed ***N*-BAP**$^+$ as a redox photosensitizer for photocatalytic CO_2 reduction in combination with BIH and **MnMes**.

Photocatalytic CO_2 reduction using *N*-BAP$^+$ and MnMes

The solution containing **MnMes** was prepared according to a reported method:[42] the corresponding MeCN complex, [Mn(6-mesityl-4,4′-dimethyl-2,2′-bipyridine)(CO)$_3$(MeCN)](PF$_6$), was dissolved in DMSO, followed by the addition of TFE and diisopropylethylamine (DIEA). TFE serves as both a CO_2-capturing reagent and a proton source in the CO_2 reduction cycle of the Mn complex. DIEA is essential for *in situ* generation of **MnMes** by coordinating deprotonated TFE to the Mn(I) center, facilitating CO_2 insertion into the Mn–O bond to form the carbonate ester complex **MnMes** (Scheme 3). This CO_2 capturing reaction increases the local concentration of CO_2 near the Mn center, enabling the efficient photocatalytic CO_2 reduction to CO even under low CO_2 concentration.

As a typical photocatalytic CO_2 reduction reaction, a CO_2-saturated DMSO solution containing ***N*-BAP**$^+$ (0.1 mM), **MnMes** (0.05 mM), BIH (0.1 M), TFE (3.78 M), and DIEA (1 vol%, 58 mM) was irradiated with LED light (λ_{max} = 430 nm). **MnMes** also exhibits UV-vis absorption in the excitation wavelength region (Fig. S6). To suppress the inner-filter effect and photodecomposition of **MnMes** during the photocatalytic reaction, we used two equivalents of the photosensitizer relative to the catalyst. Fig. 4 shows the results of the photocatalytic reaction. After 72 h of irradiation, 142 ± 15 μmol of CO was selectively produced, along with small amounts of H_2 (0.2 ± 0.1 μmol) and $HCOO^-$ (0.45 ± 0.06 μmol). The turnover number (TON) for CO production reached 1420 based on **MnMes** and 710 based on ***N*-BAP**$^+$. The absorption spectra of the reaction solutions remained nearly unchanged during the initial 8 h of the photocatalytic reaction, but underwent a substantial change after 24 h of irradiation, which correlates with the decline in the CO formation rate (Fig. S7). This suggests that the decomposition of

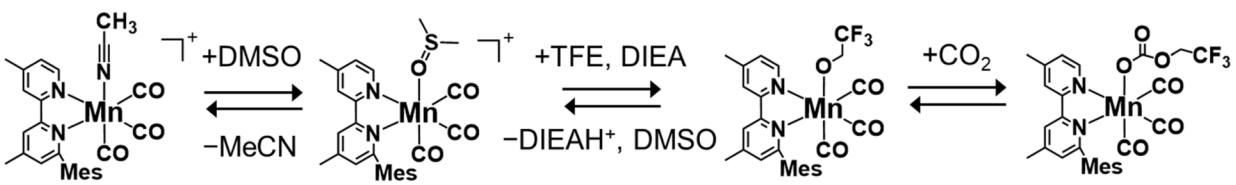

Scheme 3 Preparation of MnMes.

© 2026 The Author(s). Published by the Royal Society of Chemistry

Open Access Article. Published on 02 2026. Downloaded on 28/05/2026 05:22:51.
This article is licensed under a Creative Commons Attribution-NonCommercial 3.0 Unported Licence.

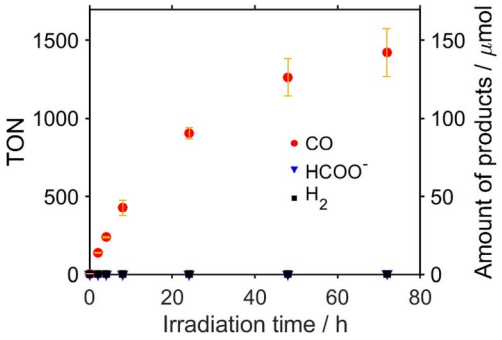

Fig. 4 Photocatalytic production of CO, $HCOO^-$, and H_2. CO_2-saturated DMSO solutions containing ***N*-BAP$^+$** (0.1 mM), **MnMes** (0.05 mM), BIH (0.1 M), TFE (3.78 M), and DIEA (58 mM) were irradiated using LED light at $\lambda_{max} = 430$ nm. TONs were calculated based on **MnMes**. The orange error bars were obtained using the results of two independent experiments.

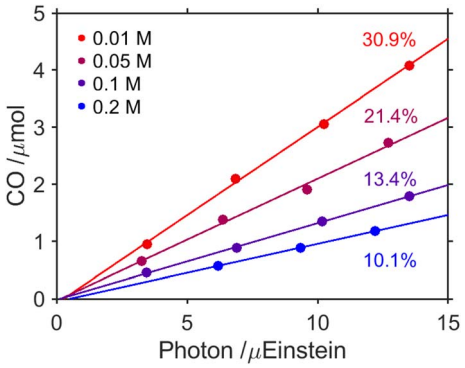

Fig. 5 Photocatalytic production of CO. CO_2-saturated DMSO solutions containing ***N*-BAP$^+$** (0.1 mM), **MnMes** (0.05 mM), BIH (0.01, 0.05, 0.1, or 0.2 M), TFE (3.78 M), and DIEA (58 mM) were irradiated using monochromatic light at 430 nm (5.0×10^{-9} einstein per s). Values represent Φ_{CO} under each condition.

***N*-BAP$^+$** is a contributing factor to the reduced photocatalytic activity, as evidenced by the significant decrease in its characteristic vibronic absorption at the final stage of the reaction (≥48 h irradiation).

Table 2 summarizes the control experiments. In the absence of ***N*-BAP$^+$**, **MnMes**, CO_2, excitation light, or BIH, no or only trace amounts of CO_2 reduction products were detected, confirming that all components are essential for the photocatalytic CO_2 reduction reaction. The small amount of CO detected in these control experiments (entry 2, 4 and 6) likely originated from the decomposition of **MnMes**, which can release up to three equivalents of CO. Although the source of the trace amounts of H_2 detected in the absence of either **MnMes** or CO_2 remains unclear, this observation clearly indicates that reduced ***N*-BAP$^+$** cannot directly transfer an electron to CO_2 and that CO formation requires the presence of CO_2. The small amounts of $HCOO^-$ and H_2 observed in the absence of BIH may result from photochemical decomposition of components in the reaction solution (entry 6). Changing the counter anion of ***N*-BAP$^+$** from Cl^- to PF_6^- had no significant effect on the photocatalytic activity, with a comparable amount of CO (128 μmol) being selectively produced and only minor amounts of H_2 (0.03 μmol) and $HCOO^-$ (0.47 μmol) formed after 72 h of irradiation.

Furthermore, the reaction was performed under a $^{13}CO_2$ atmosphere to verify the carbon source of the produced CO. The peak at $m/z = 29$, attributed to ^{13}CO, was dominant (Fig. S8a), whereas the peak at $m/z = 28$ was mainly observed in the corresponding experiment using ordinary CO_2 (Fig. S8b). Thus, CO_2 was verified to be the carbon source of the produced CO. These results demonstrate that ***N*-BAP$^+$** functions as a highly durable redox photosensitizer for photocatalytic CO_2 reduction using **MnMes** as a catalyst.

To evaluate the reaction quantum yields for CO formation (Φ_{CO}; eqn (5)), DMSO solutions containing **MnMes** (0.05 mM), ***N*-BAP$^+$** (0.1 mM), BIH, TFE (3.78 M), and DIEA (58 mM) were irradiated with a monochromatic light at 430 nm (5.0×10^{-9} einstein per s). In the presence of 0.1 M BIH, Φ_{CO} was 13.4%. Notably, Φ_{CO} increased as the BIH concentration decreased (Fig. 5), reaching a maximum of 30.9% at 0.01 M BIH. To the best of our knowledge, this is the first report demonstrating that the quantum yield of a photocatalytic CO_2 reduction reaction using a non-TADF organic photosensitizer depends on the concentration of the reductant.

$$\Phi_{CO} = \frac{\text{amount of produced CO [mol]}}{\text{amount of absorbed photon [Einstein]}} \quad (5)$$

Table 2 Control experiments excluding one of the components of the photocatalytic system

		Products/μmol (TON)[a]		
Entry[a]	Excluded component	CO	$HCOO^-$	H_2
1	—	142 ± 15 (1420 ± 150)	0.45 ± 0.06 (4.5 ± 0.6)	0.2 ± 0.1 (2 ± 1)
2	***N*-BAP$^+$**	0.41 (4.1)	N.D.	<0.1
3	**MnMes**	N.D.	N.D.	0.33 (3.3)
4[b]	CO_2	0.21 (2.1)	N.D.	0.35 (3.5)
5	Light	N.D.	N.D.	N.D.
6	BIH	0.34 (3.4)	0.29 (2.9)	0.17 (1.7)

[a] (Entry 1) as shown in Fig. 4, the photocatalytic solution was irradiated with LED light ($\lambda_{max} = 430$ nm) for 72 h. (Entries 2–6) either **MnMes** (0.05 mM), ***N*-BAP$^+$** (0.1 mM), BIH (0.1 M), CO_2, or light were excluded from the photocatalytic reactions. [b] The photocatalytic reaction was performed under Ar.

Open Access Article. Published on 02 2026. Downloaded on 28/05/2026 05:22:51.
This article is licensed under a Creative Commons Attribution-NonCommercial 3.0 Unported Licence.

Reactivities of ^{1}*N-BAP$^+$ and ^{3}*N-BAP$^+$ in the photocatalytic CO_2 reduction reactions

Since the reductive quenching of ^{1}***N*-BAP**$^+$ by BIH can compete with the ISC process (Scheme 2), the BIH concentration influences both the formation yield of ^{3}***N*-BAP**$^+$ and the quantum yields of reductive quenching for both ^{1}***N*-BAP**$^+$ ($^1\Phi_q$) and ^{3}***N*-BAP**$^+$ ($^3\Phi_q$). As shown in Fig. 5, Φ_{CO} also varies with BIH concentration. In this section, we discuss in detail the relationships among $^1\Phi_q$, $^3\Phi_q$, and Φ_{CO} based on their dependence on BIH concentration.

$^1\Phi_q$ and $^3\Phi_q$ can be expressed as functions of [BIH] as follows.

$$^1\Phi_q = \frac{^1k_q[\mathrm{BIH}]}{^1k_q[\mathrm{BIH}] + k_r + k_{nr} + k_{ISC}} \quad (6)$$

$$^3\Phi_q = \frac{k_{ISC}}{^1k_q[\mathrm{BIH}] + k_r + k_{nr} + k_{ISC}} \times \frac{^3k_q[\mathrm{BIH}]}{^3k_q[\mathrm{BIH}] + k_{r,T} + k_{nr,T}} \approx \frac{k_{ISC}}{^1k_q[\mathrm{BIH}] + k_r + k_{nr} + k_{ISC}} \quad (7)$$

where $k_{r,T}$ and $k_{nr,T}$ are the rate constants for radiative and nonradiative decay of ^{3}***N*-BAP**$^+$, respectively. The radiative and nonradiative decay of ^{3}***N*-BAP**$^+$ are much slower (τ_2 > 10 μs, Fig. 2b) than the reductive quenching of ^{3}***N*-BAP**$^+$ at [BIH] ≥ 10 mM in the photocatalytic reaction, *i.e.*, $^3k_q[\mathrm{BIH}] \gg k_{r,T} + k_{nr,T}$. Thus, $^3\Phi_q$ can be approximated as $k_{ISC}/(^1k_q[\mathrm{BIH}] + k_r + k_{nr} + k_{ISC})$. Fig. 6 illustrates the dependence of $^1\Phi_q$, $^3\Phi_q$ and Φ_{CO} on BIH concentration. Φ_{CO} shows a clear correlation with $^3\Phi_q$; both decrease as the BIH concentration increases. In contrast, $^1\Phi_q$ increases with increasing [BIH]. These results strongly indicate that the excited state primarily responsible for driving the photocatalytic CO_2 reduction reaction is ^{3}***N*-BAP**$^+$ rather than ^{1}***N*-BAP**$^+$.

Since CO is a two-electron reduction product of CO_2 and BIH acts as a two-electron donor in the photosensitized reactions (Fig. 3d),[36] the relationship among $^1\Phi_q$, $^3\Phi_q$, and Φ_{CO} is expressed in eqn (8).[15]

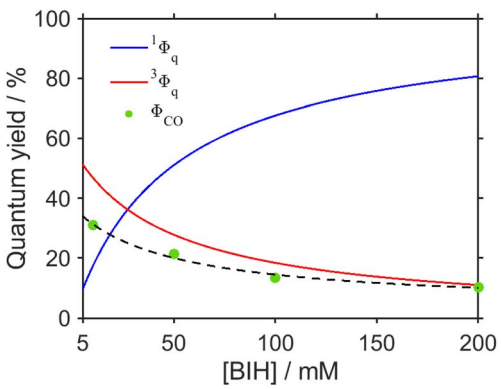

Fig. 6 Quantum yield for CO formation (Φ_{CO}), and calculated quantum yields for the reductive quenching of ^{1}*N-BAP$^+$ ($^1\Phi_q$) and ^{3}*N-BAP$^+$ ($^3\Phi_q$) as functions of BIH concentration. The black dashed line represents the fit based on eqn (8).

$$\Phi_{CO} = f \times 1/2 \times (2 \times (^1\Phi_q \times {}^1\eta_{esc} + {}^3\Phi_q \times {}^3\eta_{esc})) = f \times (^1\Phi_q \times {}^1\eta_{esc} + {}^3\Phi_q \times {}^3\eta_{esc}) \quad (8)$$

where $^1\eta_{esc}$ and $^3\eta_{esc}$ are the cage-escape yields from the singlet geminate radical pair ^{1}[***N*-BAP**$^{\bullet}$$\cdots$**BIH**$^{\bullet+}$] and the triplet geminate radical pair ^{3}[***N*-BAP**$^{\bullet}$$\cdots$**BIH**$^{\bullet+}$], which are produced *via* electron transfer between ^{1}***N*-BAP**$^+$ and BIH and between ^{3}***N*-BAP**$^+$ and BIH, respectively. The coefficient f (≤1) represents the loss in the quantum yield due to back electron transfer from ***N*-BAP**$^{\bullet}$ to **BIH**$^{\bullet+}$ by diffusive collision after escape from the geminate radical pairs and the inner filter effect of accumulated intermediates. We previously reported that, in photoinduced electron transfer reactions between several metal complexes and BIH, back electron transfer from the reduced metal complex to **BIH**$^{\bullet+}$ can be negligible because of rapid deprotonation of **BIH**$^{\bullet+}$.[38,39] Furthermore, during the photocatalytic reactions, the solutions showed no significant spectral changes at the excitation wavelength (430 nm), suggesting that the inner filter effect from accumulated intermediates was minimal (Fig. S9). Therefore, we assume that f is close to unity in our photocatalytic reaction conditions. Substituting eqn (6) and (7) into eqn (8) yields a function of Φ_{CO} with the BIH concentration as the independent variable. The experimentally observed dependence of Φ_{CO} on BIH concentration shown in Fig. 5 were fitted to this function under the assumption of $f = 1$. The fitting results are shown in Fig. 6 as a dashed line. From this fitting, $^1\eta_{esc}$ and $^3\eta_{esc}$ were estimated to be 0.035 and 0.66, respectively (Scheme 4). Notably, the triplet geminate radical pair exhibits a cage-escape yield 19 times higher than that of the singlet geminate radical pair. This is the main reason why lower BIH concentrations lead to higher CO formation quantum yields in photocatalytic reactions; at higher BIH concentrations, quenching of ^{1}***N*-BAP**$^+$ proceeds more efficiently, reducing the yield of ^{3}***N*-BAP**$^+$. We recently reported similar phenomena in photocatalytic systems using TADF molecules (**4DPAIPN** and **3DPAFIPN**), in which an equilibrium exists between singlet and triplet excited states *via* ISC and reverse ISC processes.[15] In the case of **4DPAIPN**, the escape yield of the triplet geminate radical ion pair ^{3}[**4DPAIPN**$^{\bullet-}\cdots$**BIH**$^{\bullet+}$] ($^3\eta_{esc} = 0.53$) is approximately 10 times higher than that of the singlet geminate radical ion pair. In photocatalytic reactions employing a redox photosensitizer where both singlet and triplet excited states contribute to reductive quenching by an electron donor, it can generally be concluded that improving the quantum yield for redox photosensitized reactions requires suppressing the quenching of the singlet excited state of the photosensitizer to enhance the formation yield of the corresponding triplet excited state.

Based on the above results and discussions, along with our recent reports on photocatalytic CO_2 reduction using the TADF molecules as redox photosensitizers,[15,42] we can summarize the photocatalytic CO_2 reduction mechanism in the system employing ***N*-BAP**$^+$ as the photosensitizer, as shown in Scheme 4. Although ^{1}***N*-BAP**$^+$ can be reductively quenched by BIH (particularly at higher concentrations), the yield of free ***N*-BAP**$^{\bullet}$ formation is very low because of rapid charge recombination within the singlet geminate radical pair ^{1}[***N*-BAP**$^{\bullet}$$\cdots$**BIH**$^{\bullet+}$]. At lower BIH concentrations, the ISC process becomes more

© 2026 The Author(s). Published by the Royal Society of Chemistry

Open Access Article. Published on 02 2026. Downloaded on 28/05/2026 05:22:51.
This article is licensed under a Creative Commons Attribution-NonCommercial 3.0 Unported Licence.

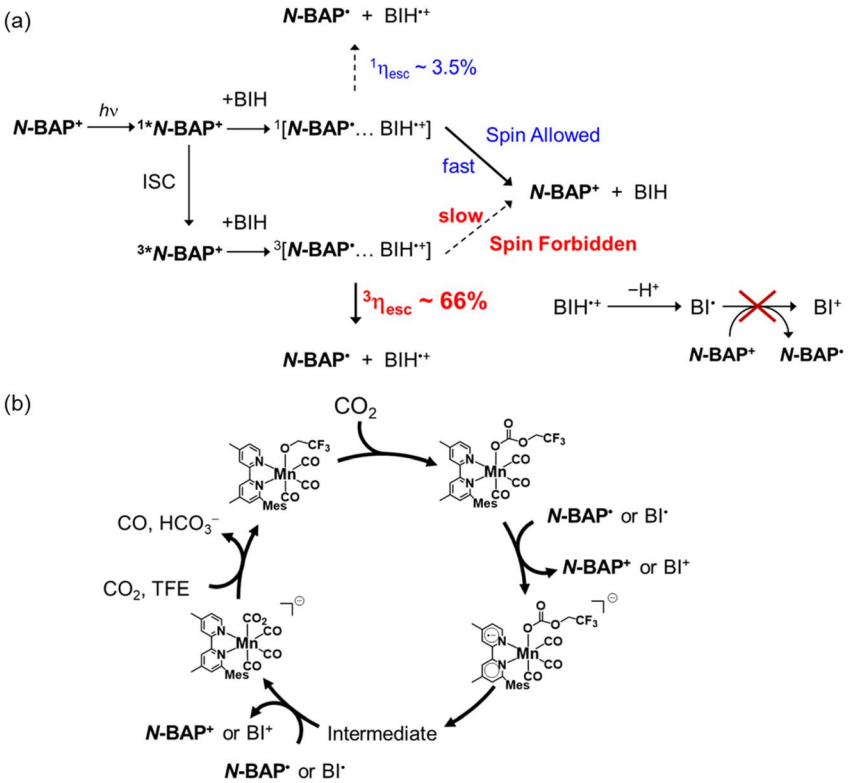

Scheme 4 Mechanism of the photocatalytic CO_2 reduction reaction: (a) reductive quenching processes of ^{1}*N-BAP$^+$ and ^{3}*N-BAP$^+$ by BIH, and (b) CO_2 reduction on the Mn–complex catalyst through electron injection processes from the reductive quenching processes.

favorable, leading to a higher concentration of ^{3}***N*-BAP$^+$**. Because reductive quenching of ^{3}***N*-BAP$^+$** proceeds efficiently even in the cases using relatively low concentration of BIH owing to its long lifetime and sufficient oxidation power, and because the escape yield of the triplet geminate radical pair ^{3}[***N*-BAP$^\bullet$⋯BIH$^{\bullet+}$**] ($^3\eta_{esc}$) is much higher than that of the singlet pair ($^1\eta_{esc}$), the dominant formation pathway for free ***N*-BAP$^\bullet$** originates from [^{3}***N*-BAP$^\bullet$⋯BIH$^{\bullet+}$**] (Scheme 4a). The resulting ***N*-BAP$^\bullet$** then initiates photocatalytic reduction of CO_2 in the Mn complex *via* single-electron transfer to **MnMes**. Oxidative quenching of the excited ***N*-BAP$^+$** by **MnMes** should be a minor process because its concentration (0.05 mM) is much lower than that of BIH (>10 mM) in the photocatalytic reaction solution. Rapid deprotonation of **BIH$^{\bullet+}$** leads to efficient formation of **BI$^\bullet$**, which serves as an additional electron donor in the photocatalytic reaction. However, because the reduction potential of **BI$^\bullet$** is less negative than that of ***N*-BAP$^+$**, **BI$^\bullet$** cannot reduce ***N*-BAP$^+$**; instead, it transfers an electron directly to **MnMes** and/or to intermediates derived from **MnMes**. Although dimerization of one-electron-reduced Mn(I) species and photochemical decomposition of the produced Mn(0) dimer typically lowers the performance of many Mn(I)–complex systems, steric hindrance from the mesityl group at the 6-position of 4,4′-dimethyl-2,2′-bipyridine completely suppresses such dimerization.[42] This structural feature is another reason for the high durability of the photocatalytic system reported herein. The intermediate(s) originating from the one-electron-reduced **MnMes** subsequently accept(s) an additional electron from **BI$^\bullet$** and/or ***N*-BAP$^\bullet$** to form [Mn(6-mesityl-4,4′-dimethyl-2,2′-bipyridine)(CO)$_3$(CO)$_2$] (**MnMes–CO$_2$**), which is a key intermediate for CO production by Mn catalysts (Scheme 4b).[42–44] Through subsequent multistep reactions, **MnMes–CO$_2$** releases CO and regenerates the original carbonate ester complex, **MnMes**, through the CO_2 capturing reaction. In this process, another CO_2 molecule might serve as an acceptor for "O^{2-}", leading to the formation of HCO_3^- in an amount equivalent to the CO produced.

From this work, the key properties required for next-generation organic photosensitizers capable of achieving high quantum yields have become evident. The first requirement is a rapid ISC to shorten the lifetime of the singlet excited state because the singlet radical pair produced *via* reductive quenching of the singlet excited state by a reductant cannot efficiently yield the free one-electron-reduced photosensitizer owing to the rapid charge recombination. Although ***N*-BAP$^+$** exhibits a relatively fast ISC rate (1.0×10^8 s^{-1}), it is still insufficient to kinetically suppress the reductive quenching of the singlet excited state. Further enhancement of the spin–orbit coupling should be required to accelerate the ISC process, for example by introducing heavy atoms, tuning the energy levels of the singlet excited states and triplet excited states, and increasing the angular momentum change associated with ISC. Another important factor is improving the cage-escape yield in the triplet-quenching process. To increase the cage-escape yield of ***N*-BAP$^+$** from 66% toward nearly 100%, it is essential to elucidate the factors that govern the cage-escape process, which

Open Access Article. Published on 02 2026. Downloaded on 28/05/2026 05:22:51. This article is licensed under a Creative Commons Attribution-NonCommercial 3.0 Unported Licence.

is influenced by multiple parameters such as the electron-transfer distance, the driving force for recombination, the noncovalent interactions between the paired radicals, and the solvent environment. Based on these principles, our research group is currently developing ***N*-BAP$^+$** derivatives with even faster ISC rates and higher $^3\eta_{esc}$.

Conclusion

4,5,9,10-Tetraethyl-1,2-dihydrobenz[*de*]imidazo[1,2,3-*ij*]-1,8-naphthridinium cation (***N*-BAP$^+$**) functions as a durable and efficient redox photosensitizer for photocatalytic CO_2 reduction. The photocatalytic system, comprising ***N*-BAP$^+$**, **MnMes**, and BIH, achieved a high turnover number of 710 based on the photosensitizer ***N*-BAP$^+$** (1420 based on the catalyst **MnMes**) and a maximum CO formation quantum yield of 30.9%. Detailed investigation of the photophysical properties of ***N*-BAP$^+$** using transient absorption spectroscopy revealed that both its singlet and triplet excited states undergo reductive quenching by BIH. Kinetic analysis demonstrated a clear correlation between Φ_{CO} and the quenching pathway: Φ_{CO} increases when the quenching pathway of the triplet excited state of ***N*-BAP$^+$** becomes dominant. This enhancement arises from the significantly higher cage-escape yield of the triplet geminate radical pair ^{3}[***N*-BAP$^{\bullet}$⋯ BIH$^{\bullet+}$**] compared to the singlet pair. The triplet geminate radical pair exhibits a cage-escape yield 19 times higher than that of the corresponding singlet pair, owing to the spin-forbidden nature of its charge recombination. The high activity of ***N*-BAP$^+$** as a redox photosensitizer can be attributed to its sufficiently high yield of triplet excited state. We have previously identified this principle in systems employing TADF-type photosensitizers.[15] This study confirms that the superiority of the triplet pathway in enhancing cage-escape efficiency is a general mechanism applicable not only to TADF-type photosensitizers but also to a broader range of organic photosensitizers that lack TADF properties. The kinetic analysis established in this study is applicable to general organic photosensitizers that do not show delayed fluorescence and thus provides a guideline for investigating the relationship between excited-state spin multiplicity and photocatalytic efficiency across a wide range of organic photosensitizers.

Experimental section

General procedures and materials

DMSO was pre-dried by adding activated 4A molecular sieves and stirring overnight under an Ar atmosphere with CaH_2. It was then vacuum-distilled at 75 °C under light shielding using an oil rotary vacuum pump. TFE was dehydrated by refluxing with Mg and I_2 for several hours prior to distillation. DIEA was dehydrated by refluxing with KOH before distillation. All solvents were stored in the dark under an Ar atmosphere after distillation. UV-vis absorption spectra were recorded using a Shimadzu UV-3600 Plus spectrophotometer. Emission spectra were measured using a Horiba Fluorolog-3-21 spectrofluorometer. Absolute photoluminescence quantum yields were determined using a Hamamatsu Quantaurus-QY Plus instrument. Emission lifetimes were measured using a Horiba FluoroCube 3000U. ^{1}H and ^{13}C NMR spectra were recorded on a JEOL JNM-ECZ400S/L1 (^{1}H at 400 MHz, ^{13}C at 101 MHz, ^{19}F at 376 MHz) spectrometer. Proton chemical shifts were referenced to the residual proton signals of the solvent at 1.94 ppm (CD_3CN). Carbon chemical shifts were referenced to the carbon signals of the solvent at 39.52 ppm (DMSO-d_6). All NMR spectra were processed using the Delta software (JEOL). IR measurements were performed on FTIR SHIMADZU Affinity-1S spectrometer fitted with a Pike Technologies MIRacle Single Reflection ATR adapter. High-resolution mass spectra were recorded on Thermo Fisher Scientific Exactive Plus (ESI).

***N*-BAP$^+$**, BIH, and **MnMes** were synthesized according to previously reported methods.[27,35,41,42] The counter anion of ***N*-BAP$^+$** was exchanged from Cl^- to PF_6^- as follows: ***N*-BAP$^+$** Cl^- (35.6 mg, 0.10 mmol) and KPF_6 (22.2 mg, 0.12 mmol, 1.2 equiv.) were placed in a Schlenk tube. The tube was sealed with a rubber septum and filled with Ar by vacuum–refill cycles (three times). CH_3CN (4.0 mL) was added to the test tube and the reaction mixture was stirred at 50 °C for 21 hours in the dark. After cooling to room temperature, the resulting mixture was washed with H_2O and dried over anhydrous $MgSO_4$. After removal of the solvent under reduced pressure, the resulting solid was washed with hexane and AcOEt, and dried *in vacuo* to give ***N*-BAP$^+$** PF_6^- (38.3 mg, 0.085 mmol, 85% yield). ^{1}H NMR (400 MHz, CD_3CN): δ = 7.92 (t, J = 8.1 Hz, 1H), 7.48 (d, J = 8.1 Hz, 2H), 4.65 (s, 4H), 2.77 (q, J = 7.5 Hz, 4H), 2.75 (q, J = 7.6 Hz, 4H), 1.25 (t, J = 7.6 Hz, 6H), 1.19 (t, J = 7.5 Hz, 6H). ^{13}C NMR (101 MHz, DMSO-d_6): δ = 148.1, 140.3, 136.7, 136.6, 120.0, 116.7, 115.9, 47.8, 21.3, 19.4, 13.3, 13.0. ^{19}F NMR (376 MHz, CD_3CN): δ = −73.4 (d, J = 706.5 Hz) (trifluoromethylbenzene was used as internal standard: δ = −63.7). HRMS (ESI$^+$): calcd for $C_{21}H_{27}N_2$, ([M]$^+$) 307.2169, found m/z 307.2163. IR (ATR): 2980 (m), 1607 (m), 1306 (m), 837 (*vs.*) cm^{-1}. Yellow solid.

Photocatalytic reactions

Photocatalytic durability (evaluated by turnover number, TON) was assessed using a merry-go-round-type photoreactor (Iris-MG, CellSystem). A 2 mL reaction solution was placed in an 11 mL test tube, purged with CO_2 for over 20 minutes, and sealed with a septum. The tube was then irradiated with 430 nm LED light inside the reactor.

Quantum yield measurements were performed using a photoreaction quantum-yield measurement system (PQY-01, Shimadzu). A 4 mL reaction solution was placed in an 11 mL quartz cuvette (1 cm optical path length), purged with CO_2 for over 20 minutes, and sealed with a septum. The solution was irradiated with monochromatic light at 430 nm. The sample temperature was maintained at 25 °C using an EYELA NCB-1210A thermostatic bath. CO and H_2 were analyzed by gas chromatography (GC-323, GL Science) using a thermal conductivity detector. Formic acid was analyzed by capillary electrophoresis (Agilent Technologies 7100 L, Otsuka Electronics).

© 2026 The Author(s). Published by the Royal Society of Chemistry

Open Access Article. Published on 02 2026. Downloaded on 28/05/2026 05:22:51. This article is licensed under a Creative Commons Attribution-NonCommercial 3.0 Unported Licence.

Transient absorption measurements

Transient absorption spectra were recorded using a UNISOKU picoTAS-ns-W2 system, equipped with a passively Q-switched microchip laser (wavelength: 355 nm; pulse width: <350 ps; pulse energy: 17 μJ per pulse) as the pump light, and a high-repetition-rate picosecond supercontinuum light source (pulse width: 50–100 ps; repetition rate: 20 MHz ± 5%) as the probe light.[45] To prevent accumulation of transient species during measurement, the sample solution was circulated through a custom-made flow cell (optical path length: 0.2 cm; see Fig. S12). UV-vis absorption spectra of the sample solution were recorded before and after TA measurements to confirm that no decomposition occurred. Global analyses were performed using Glotaran.[28]

Quantum chemical calculation

Density functional theory (DFT) calculations were performed using the Gaussian 16 package.[46] Geometry optimizations and frequency calculations were carried out using the UB3LYP functional and the 6-311++G(d,p) basis set, in conjunction with the SMD continuum solvation model for DMSO.[47] Time-dependent DFT (TD-DFT) calculations were performed in DMSO using the DFT-optimized geometry and the same functional and basis set.

Author contributions

O. I. conceived and designed the research. S. O. synthesized ***N*-BAP$^+$**. K. K. synthesized **MnMes** and BIH, and carried out photocatalytic experiments, spectroscopic measurements, and kinetic analyses. All authors contributed to supervision and manuscript preparation.

Conflicts of interest

There are no conflicts to declare.

Data availability

The data supporting this article have been included as part of the supplementary information (SI). Supplementary information is available. See DOI: https://doi.org/10.1039/d5sc08659k.

Acknowledgements

This work was supported by the Super Highway Program from JST and the Iwatani Naoji Foundation. S. O. acknowledges the financial support from JST, ACT-X grant number JPMJAX23D6, and JSPS KAKENHI grant numbers JP24H01873 (Green Catalysis Science) and JP24K17688 (Early-Career Scientists). The authors thank Y. Norisada for his help in preparing *N*-BAP$^+$PF$_6^-$. K. K. acknowledges financial support from Hiroshima Carbon Recycling Young Researchers Support Program. The computation was carried out using the computer resources offered under the category of Comprehensive Projects between Hiroshima University and Kyushu University by Research Institute for Information Technology, Kyushu University.

References

1 S. Fang, M. Rahaman, J. Bharti, E. Reisner, M. Robert, G. A. Ozin and Y. H. Hu, *Nat. Rev. Methods Primers*, 2023, **3**, 61.
2 S. Berardi, S. Drouet, L. Francàs, C. Gimbert-Suriñach, M. Guttentag, C. Richmond, T. Stoll and A. Llobet, *Chem. Soc. Rev.*, 2014, **43**, 7501–7519.
3 Y.-J. Yuan, Z.-T. Yu, D.-Q. Chen and Z.-G. Zou, *Chem. Soc. Rev.*, 2017, **46**, 603–631.
4 C. Bizzarri, *Eur. J. Org Chem.*, 2022, **2022**, e202200185.
5 Y. Yamazaki, H. Takeda and O. Ishitani, *J. Photochem. Photobiol., C*, 2015, **25**, 106–137.
6 Y. Wu, D. Kim and T. S. Teets, *Synlett*, 2022, **33**, 1154–1179.
7 N. A. Romero and D. A. Nicewicz, *Chem. Rev.*, 2016, **116**, 10075–10166.
8 M. H. Shaw, J. Twilton and D. W. C. MacMillan, *J. Org. Chem.*, 2016, **81**, 6898–6926.
9 C. K. Prier, D. A. Rankic and D. W. C. Macmillan, *Chem. Rev.*, 2013, **113**, 5322–5363.
10 M. A. Bryden and E. Zysman-Colman, *Chem. Soc. Rev.*, 2021, **50**, 7587–7680.
11 Y. Wang, X.-W. Gao, J. Li and D. Chao, *Chem. Commun.*, 2020, **56**, 12170–12173.
12 E. Bassan, R. Inoue, D. Fabry, F. Calogero, S. Potenti, A. Gualandi, P. G. Cozzi, K. Kamogawa, P. Ceroni, Y. Tamaki and O. Ishitani, *Sustain. Energy Fuels*, 2023, **7**, 3454–3463.
13 E. Speckmeier, T. G. Fischer and K. Zeitler, *J. Am. Chem. Soc.*, 2018, **140**, 15353–15365.
14 N. H. Damrauer, G. Cerullo, A. Yeh, T. R. Boussie, C. V. Shank and J. K. McCusker, *Science*, 1997, **275**, 54–57.
15 Y. Tamaki, K. Kamogawa, R. Inoue, P. Ceroni and O. Ishitani, *J. Am. Chem. Soc.*, 2025, **147**, 33010–33022.
16 M. J. Goodwin, J. C. Dickenson, A. Ripak, A. M. Deetz, J. S. McCarthy, G. J. Meyer and L. Troian-Gautier, *Chem. Rev.*, 2024, **124**, 7379–7464.
17 Z. Guo, S. Cheng, C. Cometto, E. Anxolabehere-Mallart, S. M. Ng, C. C. Ko, G. Liu, L. Chen, M. Robert and T. C. Lau, *J. Am. Chem. Soc.*, 2016, **138**, 9413–9416.
18 L. Chen, Y. Qin, G. Chen, M. Li, L. Cai, Y. Qiu, H. Fan, M. Robert and T.-C. Lau, *Dalton Trans.*, 2019, **48**, 9596–9602.
19 Q. Lei, H. Yuan, J. Du, M. Ming, S. Yang, Y. Chen, J. Lei and Z. Han, *Nat. Commun.*, 2023, **14**, 1087.
20 M. Kientz, G. Lowe, B. G. McCarthy, G. M. Miyake, J. Bonin and M. Robert, *ChemPhotoChem*, 2022, **6**, e202200009.
21 H. Rao, C. H. Lim, J. Bonin, G. M. Miyake and M. Robert, *J. Am. Chem. Soc.*, 2018, **140**, 17830–17834.
22 H. Gao, G. Liu, Y. Zhu, Z. Wen, X. Liu, G. Wang and F. Li, *Green Chem. Eng.*, 2023, **4**, 433–438.
23 X. Chen, Y. Wei, W. Sun, X. Meng, S. Hao and Y. Gao, *Mol. Catal.*, 2021, **500**, 111299.
24 S. Hao, K.-K. Chen, P. Liang, Q. Huang, L. Zhou, Y. Wei and Z. Wei, *Nat. Commun.*, 2025, **16**, 6167.

Open Access Article. Published on 02 2026. Downloaded on 28/05/2026 05:22:51.
This article is licensed under a Creative Commons Attribution-NonCommercial 3.0 Unported Licence.

25 P.-Y. Ho, S.-C. Cheng, F. Yu, Y.-Y. Yeung, W.-X. Ni, C.-C. Ko, C.-F. Leung, T.-C. Lau and M. Robert, *ACS Catal.*, 2023, **13**, 5979–5985.
26 S. Hao, Z. Wang, K.-K. Chen, Y. Wei, L. Zhou and Z. Wei, *ChemCatChem*, 2025, **17**, e00733.
27 S. Okumura, S. Hattori, L. Fang and Y. Uozumi, *J. Am. Chem. Soc.*, 2024, **146**, 16990–16995.
28 J. J. Snellenburg, S. Laptenok, R. Seger, K. M. Mullen and I. H. M. van Stokkum, *J. Stat. SoftwareJ. Stat. Software*, 2012, **49**, 1–22.
29 I. H. M. van Stokkum, D. S. Larsen and R. van Grondelle, *Biochim. Biophys. Acta, Bioenerg.*, 2004, **1657**, 82–104.
30 S. Neumann, C. Kerzig and O. S. Wenger, *Chem. Sci.*, 2019, **10**, 5624–5633.
31 C. Wang, H. Li, T. H. Bürgin and O. S. Wenger, *Nat. Chem.*, 2024, **16**, 1151–1159.
32 P. Müller and K. Brettel, *Photochem. Photobiol. Sci.*, 2012, **11**, 632–636.
33 A. W. Adamson and J. N. Demas, *J. Am. Chem. Soc.*, 1971, **93**, 1800–1801.
34 E. Hasegawa, S. Takizawa, T. Seida, A. Yamaguchi, N. Yamaguchi, N. Chiba, T. Takahashi, H. Ikeda and K. Akiyama, *Tetrahedron*, 2006, **62**, 6581–6588.
35 E. Hasegawa, T. Seida, N. Chiba, T. Takahashi and H. Ikeda, *J. Org. Chem.*, 2005, **70**, 9632–9635.
36 Y. Tamaki, K. Koike, T. Morimoto and O. Ishitani, *J. Catal.*, 2013, **304**, 22–28.
37 S. Okumura, T. Imuta, K. Kato, K. Shimosaka, H. Aoki, Y. Aoyagi, K. Hikichi and N. Ishida, *Chem. Lett.*, 2025, **54**, upaf135.
38 N. Hosokawa, K. Ozawa, K. Koike, Y. Tamaki and O. Ishitani, *Chem. Sci.*, 2025, **16**, 4279–4289.
39 K. Ozawa, Y. Tamaki, K. Kamogawa, K. Koike and O. Ishitani, *J. Chem. Phys.*, 2020, **153**, 154302.
40 K. Kamogawa, Y. Shimoda, K. Miyata, K. Onda, Y. Yamazaki, Y. Tamaki and O. Ishitani, *Chem. Sci.*, 2021, **12**, 9682–9693.
41 X. Q. Zhu, M. T. Zhang, A. Yu, C. H. Wang and J. P. Cheng, *J. Am. Chem. Soc.*, 2008, **130**, 2501–2516.
42 K. Kamogawa, H. Koizumi and O. Ishitani, *J. Am. Chem. Soc.*, 2025, **147**, 39284–39297.
43 K. T. Ngo, M. McKinnon, B. Mahanti, R. Narayanan, D. C. Grills, M. Z. Ertem and J. Rochford, *J. Am. Chem. Soc.*, 2017, **139**, 2604–2618.
44 C. Riplinger, M. D. Sampson, A. M. Ritzmann, C. P. Kubiak and E. A. Carter, *J. Am. Chem. Soc.*, 2014, **136**, 16285–16298.
45 T. Nakagawa, K. Okamoto, H. Hanada and R. Katoh, *Opt. Lett.*, 2016, **41**, 1498–1501.
46 M. J. Frisch, G. W. Trucks, H. B. Schlegel, G. E. Scuseria, M. A. Robb, J. R. Cheeseman, G. Scalmani, V. Barone, G. A. Petersson, H. Nakatsuji, X. Li, M. Caricato, A. V. Marenich, J. Bloino, B. G. Janesko, R. Gomperts, B. Mennucci, H. P. Hratchian, J. V. Ortiz, A. F. Izmaylov, J. L. Sonnenberg, D. Williams-Young, F. Ding, F. Lipparini, F. Egidi, J. Goings, B. Peng, A. Petrone, T. Henderson, D. Ranasinghe, V. G. Zakrzewski, J. Gao, N. Rega, G. Zheng, W. Liang, M. Hada, M. Ehara, K. Toyota, R. Fukuda, J. Hasegawa, M. Ishida, T. Nakajima, Y. Honda, O. Kitao, H. Nakai, T. Vreven, K. Throssell, J. A. Montgomery Jr, J. E. Peralta, F. Ogliaro, M. J. Bearpark, J. J. Heyd, E. N. Brothers, K. N. Kudin, V. N. Staroverov, T. A. Keith, R. Kobayashi, J. Normand, K. Raghavachari, A. P. Rendell, J. C. Burant, S. S. Iyengar, J. Tomasi, M. Cossi, J. M. Millam, M. Klene, C. Adamo, R. Cammi, J. W. Ochterski, R. L. Martin, K. Morokuma, O. Farkas, J. B. Foresman and D. J. Fox, *Gaussian 16 Rev. C.01*, Gaussian, Inc., Wallingford CT, 2016.
47 A. V. Marenich, C. J. Cramer and D. G. Truhlar, *J. Phys. Chem. B*, 2009, **113**, 6378–6396.

© 2026 The Author(s). Published by the Royal Society of Chemistry